Insights into amorphous low-density hydrous RuO2 for supercapacitors using ab initio molecular dynamics simulations

Hicham Jabraoui, David Pech, Mehdi Djafari Rouhani, Carole Rossi, Alain Esteve

▶ **To cite this version:**

Hicham Jabraoui, David Pech, Mehdi Djafari Rouhani, Carole Rossi, Alain Esteve. Insights into amorphous low-density hydrous RuO2 for supercapacitors using ab initio molecular dynamics simulations. Journal of Energy Storage, 2024, 98, pp.112926. 10.1016/j.est.2024.112926 . hal-04774640

HAL Id: hal-04774640
https://laas.hal.science/hal-04774640v1

Submitted on 8 Nov 2024

HAL is a multi-disciplinary open access archive for the deposit and dissemination of scientific research documents, whether they are published or not. The documents may come from teaching and research institutions in France or abroad, or from public or private research centers.

L'archive ouverte pluridisciplinaire **HAL**, est destinée au dépôt et à la diffusion de documents scientifiques de niveau recherche, publiés ou non, émanant des établissements d'enseignement et de recherche français ou étrangers, des laboratoires publics ou privés.

Insights into Amorphous Low-Density Hydrous RuO_2 for Supercapacitors using *ab initio* Molecular Dynamics Simulations

Hicham Jabraoui,* David Pech, Mehdi Djafari Rouhani, Carole Rossi, and Alain Esteve*

LAAS-CNRS, University of Toulouse, CNRS, 7 avenue du Colonel Roche, 31400 Toulouse, France.

E-mail: hicham.jabraoui@gmail.com; aesteve@laas.fr

Abstract

Hydrated ruthenium dioxide (RuO_2) stands out as the archetype of pseudocapacitive materials, renowned for its outstanding capacitance and remarkable stability for supercapacitor applications. Herein, we introduce a model of amorphous low-density hydrous RuO_2 for supercapacitors, utilizing a combined approach of *ab initio* molecular dynamics simulations (AIMD) and density functional theory (DFT), along with Nudged Elastic Band (NEB) methods, making the first instance of such an approach. Starting from an anhydrous amorphous structure, we systematically increase hydration levels within the model. Our simulations reveal the critical role of OH groups at oxygen non−bridging sites and molecular water in enhancing hydrogen mobility. Furthermore, the presence of water facilitates the Grotthuss mechanism, forming a ring of H−bond donors and acceptors involving water and oxygen. This mechanism connects distant sites, creating multiple pathways for hydrogen migration within the system, with an activation range of 0.3−0.4 eV. These findings provide valuable insights into the behavior of hydrated RuO_2 in supercapacitors, shedding light on the interplay between hydration and hydrogen motion for enhanced energy storage applications.

INTRODUCTION

Supercapacitors, also known as electrochemical capacitors, have emerged as promising energy storage devices due to their exceptional power density and rapid charge− discharge capabilities.[1–3] They bridge the gap between conventional capacitors and batteries, offering a unique solution for various applications, including portable electronics, renewable energy systems, and electric vehicles.[4] One of the key factors driving the advancement of supercapacitor technology is the development of new electrode materials with enhanced energy storage capabilities. Pseudocapacitive materials, unlike conventional capacitive materials, store energy through fast and reversible Faradaic redox reactions at the electrode−electrolyte interface.[5] This distinctive mechanism allows pseudocapacitors to achieve higher energy densities than their capacitive counterparts. Among pseudocapacitive materials, ruthenium dioxide (RuO_2) distinguishes itself as the quintessential example, embodying unparalleled electrochemical characteristics. While anhydrous crystalline RuO_2 show moderate capacitance (a few tens of $F.g^{-1}$), the hydrous form of RuO_2 allows increasing the capacitance by several orders of magnitude, reaching values in the range of several hundreds to thousands of F.g⁻1. Experimental studies have consistently demonstrated that amorphous (~2.3 $g.cm^{-3}$)) low−density hydrous RuO_2 outperforms its crystalline counterpart in terms of specific capacitance and cycle stability.[6,7] However, the underlying reasons for this superior electrochemical performance remain a subject of ongoing research.

Hydrous RuO_2 is typically obtained through electrochemical means resulting in a lowering of the overall material density as compared to defect−less crystalline RuO_2. The exceptional performance demonstrated by electrodes based on amorphous, low−density hydrous RuO_2 has spurred significant research efforts, particularly in the realm of materials characterization. Various techniques, including electron microscopy,[8] X−ray spectroscopy,[9] X−ray atomic pair distribution function (PDF) analysis,[10,11] and nuclear magnetic resonance (NMR),[12] have been employed to investigate the structure of hydrous RuO_2. These studies have revealed crucial information about the composition and bonding within this ma-

terial. For instance, X−ray PDF analysis has shown that $RuO_2{\cdot}xH_2O$ consists of anhydrous rutile−like RuO_2 nanocrystals dispersed within a matrix of structural water associated with Ru−−O bonds.[10,11] NMR studies, particularly those conducted by Fu *et al.*[13] have provided insights into proton motion and hydrogen bonding in RuO_2. They found that the proton dynamics in $RuO_2{\cdot}xH_2O$ samples are temperature−dependent, where higher temperatures facilitate easier proton diffusion. Furthermore, they reported activation energy (E_a) values for proton diffusion in hydrous RuO_2, ranging approximately from 0.265 to 0.181 eV. Despite these findings achieving a comprehensive understanding of the relationship between electrical performance, local structural details and transport properties of $RuO_2{\cdot}xH_2O$ remains elusive due to its non−crystalline nature and variable chemistry making characterisation difficult. Only a few attempts have been made to establish a fundamental understanding from a theoretical standpoint. Atomic−scale modeling of RuO_2 has primarily been limited to considerations derived from its crystalline state.[14–18] As far as our current knowledge is concerned, no theoretical investigations attempting to understand hydrousRuO_2 have been conducted to date.

To address these questions, we employ *ab initio* molecular dynamics simulations to create and analyze, for the first time, a model system of amorphous low−density hydrous RuO_2. These structural models are juxtaposed with fully dense and crystalline RuO_2, examining aspects such as the distribution of pores, spatial distribution of polyhedral, and Ru oxidation states. Then the hydration level and water inclusion in the porous system are adjusted by varying the water content to investigate the protonic arrangement within the inhomogeneous structure. This allows investigating and quantifying the various scenario of hydrogen migration, governing its exceptional pseudocapacitive behavior.

Computational details

Generation of amorphous RuO_2 model structures

Low density (2.2 g.cm^{-3}) and fully dense (6.3 g.cm^{-3}) anhydrous amorphousRuO_2 model structures were firstly created for comparison purposes before hydration. Standard melt−quench procedures through classical molecular dynamics simulation[19–21] were firstly employed to obtain an initial atomic distribution,comprising 24 Ru and 48 O atoms, in a stoichiometric orthorhombic cell (with dimensions 20.00 × 9.73 × 12.32 Å^3) (*cf.* details in SI). This process resulted in a low−density model structure with an equivalent RuO_2 mass density of 2.21 g.cm^{-3}, **i.e** close to the experimental measured density of hydrous RuO_2.[6] The structure acquired at room temperature from classical MD simulations served as the input for *ab initio* MD simulations based on the Born−Oppenheimer approximation, conducted using the Vienna *ab initio* Simulation Package (VASP,[22]). The methodology applied in this study is adapted from our previous work, facilitating the realization of a realistic glassy state, especially for more intricate compositions such as calcium−sodium borosilicate glasses.[21] MD simulations based on DFT are recognized for their ability to more accurately reproduce experimental results compared to force field−based simulations, which is crucial for capturing the proper polyhedral distribution in bulk and surface structures.[21,23] In this work, we used the GGA−PBE functional,[24] which includes D2 dispersion corrections[25] to account for long−range van der Waals interactions. The projector−augmented wave (PAW) method was utilized, and a plane−wave cutoff energy of 450 eV was employed. The MD procedure proceeded as the following steps: (i) the obtained classical molecular dynamics (MD) atomic distribution was initially heated to 2500 K with an NVT run of 15 ps, (ii) followed by an NVE run lasting 10 ps to equilibrate the system in the liquid state, and finally, (iii) the system was quenched to 300 K over 10 ps. The MD timestep was set to 1.0 fs. For direct comparison purpose, a fully dense and amorphous reference RuO_2 was constructed using the same orthorombic unit−cell, and following a similar procedure, but

considering an additional step: a relaxation in an NPT run at 300 K to equilibrate the system at the glass density (5 ps), followed by a final NVE run at 300 K to further equilibrate the structure at the mean density, determined from the last ps of the NPT run. A density of 6.31 g.cm^{-3} was achieved for this structure,approximating the density of crystallineRuO$_2$ (7.07 g.cm^{-3}). Note that a Nosé−Hoover thermostat and barostat were employed to control the temperature during BOMD simulations. Subsequently, we allowed the system to relax under the NVT ensemble for 20 ps at the same temperature. Figure 1 shows snapshots of both the simulated low−density amorphous RuO$_2$ structure and the simulated fully−dense amorphous RuO$_2$ structure.

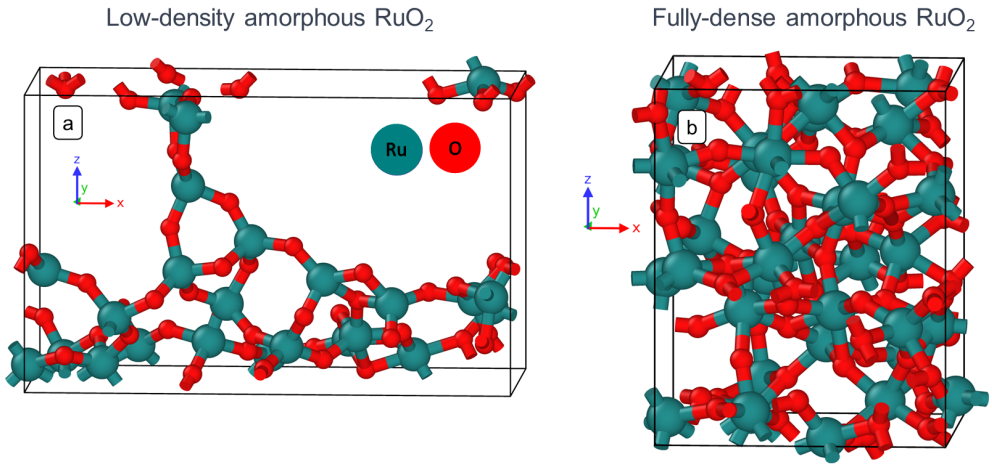

Figure 1: Snapshots of the AIMD−obtained (a) low−density amorphous RuO$_2$ and (b) fully−dense amorphous RuO$_2$ structures at 300 K. Green balls represent Ru atoms, and red balls represent O atoms.

Generation of the hydrous form of low density RuO$_2$

We utilized the same VASP package with identical parameters as previously employed to simulate hydrous RuO$_2$. Our simulations encompass the exploration of both low−density amorphous structures and porous amorphous structures of hydrated RuO$_2$ for which non−dissociated water molecules can exist. To enable the accurate representation of potential Grotthuss mechanisms during MD simulations, we reduced the MD timestep to 0.5 fs, as detailed in.[26] Additionally, hydrogen atoms were replaced with deuterium atoms to ensure

adiabaticity within the Born−Oppenheimer Molecular Dynamics (BOMD) simulations.

Hydration of the dry low−density structure (as obtained from AIMD) was performed first, introducing three different amounts of water molecules, *e.g.*, 19, 29, and 39 water molecules, into the pores. Hydration was further carried out at three different temperatures: 350 K, 450 K, and 550 K. Initially, to facilitate rapid equilibration, we conducted an NVE ensemble simulation for 10 ps, followed by a 60 ps simulation at the target temperature in the NVT ensemble. In the initial stage, water molecules were carefully distributed to allow adsorption *via* their oxygen atom onto the low coordination Ru sites, specifically Ru^{III} and Ru^{IV} sites of the dry RuO_2. Furthermore, we directly separated some water molecules to position hydrogen on O bridging sites being under−coordinated (exhibiting only two bonds with Ru atoms). This was based on insights from a preliminary DFT investigation aimed at identifying the most stable sites. Extra water molecules, dealing with higher initial quantities, were positioned into the pores at the second and third layer away from the hydrated RuO_2 walls.

Detailed hydration and migrations mechanisms *via* static DFT calculations

Density Functional Theory (DFT) calculations were performed using the VASP package, employing the PBE density functional and the projector−augmented wave (PAW) approach, with a plane−wave cutoff energy of 450 eV. For each calculation, atomic positions were relaxed until the forces acting on each atom were below 0.02 eV/Å. Brillouin zone sampling was limited to the Γ point. To account for van der Waals interactions, the semi−empirical D2 method developed by Grimme[25] was employed. This level of computational theory has demonstrated effectiveness in prior studies involving the hydration of mineral surfaces.[21,26] To simulate migration pathways and calculate activation energies of protons within low−density amorphous RuO_2 hydrous structures, we utilized the nudged elastic band (NEB) technique,[27,28] including six intermediate images between the initial and final configurations.

The activation energy (E_a) was defined as the energy difference between a given (meta)stable configuration and the saddle point in energy that must be overcome to transition to another neighboring (meta)stable configuration.

Results and Discussion

Dry amorphous low density RuO_2

Ruthenium dioxide (RuO_2) manifests in various crystallographic forms, with the rutile structure being one of the well−known variations.[29,30] Besides the rutile (*P42/mnm*) and orthorhombic (*$CaCl_2$-type*) structures,[31] RuO_2 can also adopt an amorphous state without a defined atomic structure over extended ranges. This study primarily focuses on investigating the amorphous state, which, to the best of our knowledge, has not been theoretically documented before. We first consider a dry amorphous and low density RuO_2 (2.21 g.cm^{-3}) model system to provide better understanding of its hydrous form after hydration. The low density material will also be compared to reference fully−dense amorphous having a density of 6.31 g.cm^{-3} and crystalline RuO_2 (density of 7.07 g.cm^{-3} [32]), as illustrated in Figure 1 and summarized in Table 1.

The morphological differences between the two amorphous states are significant. The fully−dense variant is predominantly composed of two distinct ring sizes, three and four (Ru−−Ru, homopolar bonds).[33] In contrast, the low−density amorphous phase of RuO_2 exhibits significant porosity, with ring sizes extending up to 17 (see Figure S1). Distinguishing between the crystalline and amorphous states requires characterizing the oxygen state of Ru. In the crystalline state, Ru solely exists as Ru^{VI} (100%) with Ru−−O at 1.92 and 2.00 Å, O−−O at 2.52 Å, and Ru−−Ru at 3.11 Å, as well as $\theta_{O-Ru-O}(^\circ)$ of 76.82 and 103.18 and $\theta_{Ru-O-Ru}(^\circ)$ of 128.41 (see Table 2 and [32]). Upon transitioning to the fully dense amorphous states of RuO_2, two distinct Ru oxygen oxidation states coexist, Ru^{V} at 29.40% and Ru^{V} at 70.60%. The corresponding Ru−−O distance is 1.97± 0.03 Å , O−−O ranges

from 2.43 Å to 2.78 Å, and Ru——Ru extends from 3.13 Å to 3.63 Å, as well as $\theta_{O-Ru-O}(^{\circ})$ of 77−97 and $\theta_{Ru-O-Ru}(^{\circ})$ of 103−137 (see Table 2).

In contrast, the low−density structure of RuO_2displays three distinct oxygen oxidation states for Ru: Ru^{III} at 4.2%, Ru^{IV} at 79.20%, and Ru^{V} at 16.60%. The Ru——O distances range from 1.85 ± 0.03 Å, O——O ranges from 2.85 Å to 3.15 Å, and Ru——Ru ranges from 3.1 Å to 3.55 Å, as well as $\theta_{O-Ru-O}(^{\circ})$ of 77−133 and $\theta_{Ru-O-Ru}(^{\circ})$ of 95−135 (as indicated in Table 2). Importantly, the transition from the crystalline to the amorphous state involves a reduction in the oxygen oxidation state, with the lowest oxidation state of Ru observed in the low−density structure of RuO_2. These findings are consistent with previous experimental investigations using various techniques, including thermogravimetric analysis (TGA), X−ray diffraction (XRD), and X−ray absorption near−edge structure (XANES) and extended X−ray fine structure (EXAFS) analyses. However, it is important to note that XANES cannot distinguish between Ru^{III} and Ru^{IV} in the hydrous oxides.[9]

Comparing the three systems, the highly ordered crystalline structure of RuO_2 exhibits a uniform distribution of the Ru^{VI} oxidation state along with a denser atomic packing. In contrast, the fully−dense amorphousRuO_2 manifests a significant presence of Ru^{V} content, indicating a greater degree of oxygen deficiency and structural disorder. Notably, the presence of distinct ring sizes, indicative of homopolar bonds, underlines the formation of a more intricate network within the fully−dense amorphous phase. On the other hand, the amorphous low−density RuO_2 system displays a remarkable diversity in Ru oxidation states, with a substantial proportion of Ru^{III} and Ru^{IV}, indicating a higher level of structural flexibility and oxygen incorporation. Additionally, the extensive porosity observed in the low-density amorphous phase suggests the presence of interconnected voids, enabling enhanced ion diffusion and accessibility, which are crucial factors for its potential application in energy storage systems.

Table 1: Characteristics of RuO_2 in different states described in terms of density, interatomic distances, Ru polyhedra, coordination numbers (CN), and angles. Interatomic distances within the first shell, including Ru−O, O−O, and Ru−Ru distances and $\theta_{Ru-O-Ru}(^\circ)$, $\theta_{O-Ru-O}(^\circ)$ angles, are obtained from radial distribution function (RDF) and angle distribution function (ADF) analysis. Meanwhile, the latter and Ru oxidation states for a radius over 2.3 Å are calculated over the last 10 ps.

Crystalline (Rutile)[32]			
Density (g.cm^{-3})	**Ru**^{III}(%)	**Ru**^{IV}(%)	**Ru**^{V}(%)
7.07	0	0	0
Ru^{VI}(%)	**CN**$_{Ru-O}$	$\theta_{Ru-O-Ru}(^\circ)$	$\theta_{O-Ru-O}(^\circ)$
100	6	128.41	76.82 and 103.18
r_{Ru-O}(**Å**)	r_{O-O}(**Å**)	r_{Ru-Ru}(**Å**)	−−
1.92 and 2.00 ± 0.01	2.52	3.11	−−
Amorphous (Fully−dense)			
Density (g.cm^{-3})	**Ru**^{III}(%)	**Ru**^{IV}(%)	**Ru**^{V}(%)
6.31	0.00	0.00	29.40
Ru^{VI}(%)	**CN**$_{Ru-O}$	$\theta_{Ru-O-Ru}(^\circ)$	$\theta_{O-Ru-O}(^\circ)$
70.60	5.76	103−137	77−97
r_{Ru-O}(**Å**)	r_{O-O}(**Å**)	r_{Ru-Ru}(**Å**)	−−
1.97 ± 0.03	2.43−2.78	3.13−3.63	−−
Amorphous (Low Density)			
Density (g.cm^{-3})	**Ru**^{III}(%)	**Ru**^{IV}(%)	**Ru**^{V}(%)
2.21	4.20	79.20	16.60
Ru^{VI}(%)	**CN**$_{Ru-O}$	$\theta_{Ru-O-Ru}(^\circ)$	$\theta_{O-Ru-O}(^\circ)$
0	4.21	95−135	77−133
r_{Ru-O}(**Å**)	r_{O-O}(**Å**)	r_{Ru-Ru}(**Å**)	−−
1.85± 0.03	2.85−3.15	3.1−3.55	−−

Hydrated form of amorphous and low density RuO_2

With the aim of establishing model systems of the amorphous hydrous RuO_2 material, we varied the hydration levels of the dry, low density RuO_2 by incorporating three different quantities of water molecules (19 H_2O, 29 H_2O, and 39 H_2O into RuO_2, as detailed in the "Computational details" section. These configurations were relaxed at three different temperatures: 350 K, 450 K, and 550 K. Figure 2 presents snapshots of the resulting low density structure after the relaxation process at 550 K, over 60 ps. In Figure 2a the case without hydration (0 H_2O) is shown, while Figure 2b , Figure 2c and Figure 2d represent the structure obtained after hydration with exposures to 19 H_2O, 29 H_2O and 39 H_2O, respectively. The systematic introduction of water initiates dissociation reactions, generating OH species on the porous surface. In the case of 19 H_2O at 550 K, only one water molecule remains within the pore, while this amount increases with higher initial water content. Different OH species configurations coexist, namely Non Bridging Oxygen (NBO), where OH is bonded solely to one ruthenium atom, and Bridging Oxygen (BO), where oxygen bonded to hydrogen shares chemical bonds with two ruthenium atoms. The distribution of NBO results in isolated, vicinal or geminated hydroxyls. Quantification of species in the hydrated structure is given in Table 2. Importantly, at 550 K, the hydration process remains at saturation as the percentage of OH (relative to the total number of Ru atoms) is constant (117%) at all considered initial water content. This implies that the proposed hydrous RuO_2 structure at 550 K is characterized by a quantity of OH sites exceeding the number of Ru atoms. Further water content will depend on the initial loading. While the hydration level slightly varies as a function of the relaxation temperature, the variation is $non-linear$ (see Table 2, OH % variation from 350 to 550 K). It has to be noted that the hydration level remains high in the lower loading case (19 H_2O). Furthermore, no hydrogen is found in oxygen connected to three Ru atoms.

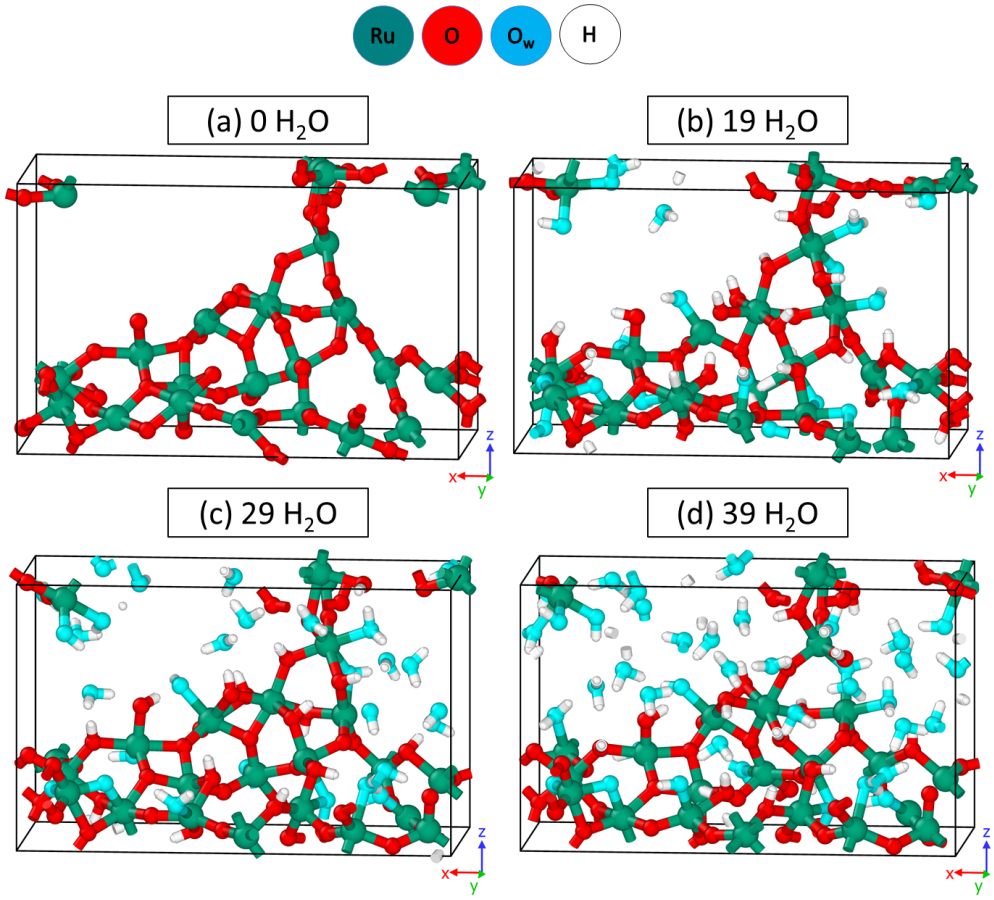

Figure 2: Amorphous hydrated RuO_2 after undergoing low−density relaxation at 550K over 60 ps: (a) for 0 H_2O, (b) for 19 H_2O, (c) for 29 H_2O, and (d) for 29 H_2O molecules. Green balls represent Ru atoms, red balls represent O atoms initially part of RuO_2, blue balls represent O atoms initially part of H_2O, and white balls represent H atoms.

Examining the ruthenium oxidation states in Figure 3,we observe a clear increase in the oxidation state of Ru after all three hydration processes, in comparison to the dehydrated low−density RuO_2. The previously observed Ru^{III} oxidation state is no longer present, replaced by the noticeable appearance of Ru^{VI}. Concerning the influence of water content, the percentage of Ru^{V} continues to rise from 34% to 63%, whereas the percentage of the lowest oxidation state of Ru^{IV} decreases from 50% to 26%, as illustrated in Figure 3. Overall, this leads to a slight decrease in the average coordination number of Ru with respect to oxygen, from 5.4 (19 H_2O) to 5.1 (for 29 and 39 H_2O). Logically, the Ru−−O interatomic distance is shown to decrease, being 1.92 Å for 19H_2O, then decreasing to 1.90Å for 29H_2O and 1.89Å

for $29H_2O$. It is worth noting that the lowest coordination obtained for the de−hydrated RuO_2 exhibits an even more contracted bond length, to 1.85 Å(Table 2). Focusing on the impact of the relaxation temperature used for RuO_2 model elaboration, the lowest oxidation state (Ru^{IV}) and the highest oxidation state (Ru^{VI}) increase as the temperature decreases, while the intermediate oxidation state (Ru^{V}) decreases with increasing temperature, from 63% to 74%. Again, the average coordination number of Ru with respect to oxygen remains constant at 5.1 highlighting the robust nature of the structural framework of RuO_2 in response to temperature fluctuations. While the overall hydration remains stable, specifically constant upon water loading at 550 K (117% OHs), and slightly fluctuating with increasing the temperature (in the range of 100 to 117%), the coordination being itself also quasi constant, net tendencies on the amounts of both BO and NBO are observed. An increase in water loading or temperature results in a rise in the amount of NBO while BO amount decreases. Notably, the NBO configuration is entirely absent from the de−hydrated structure. The balance of OH species configurations might influence hydrogen migration within the RuO_2 model structures, which will be addressed next.

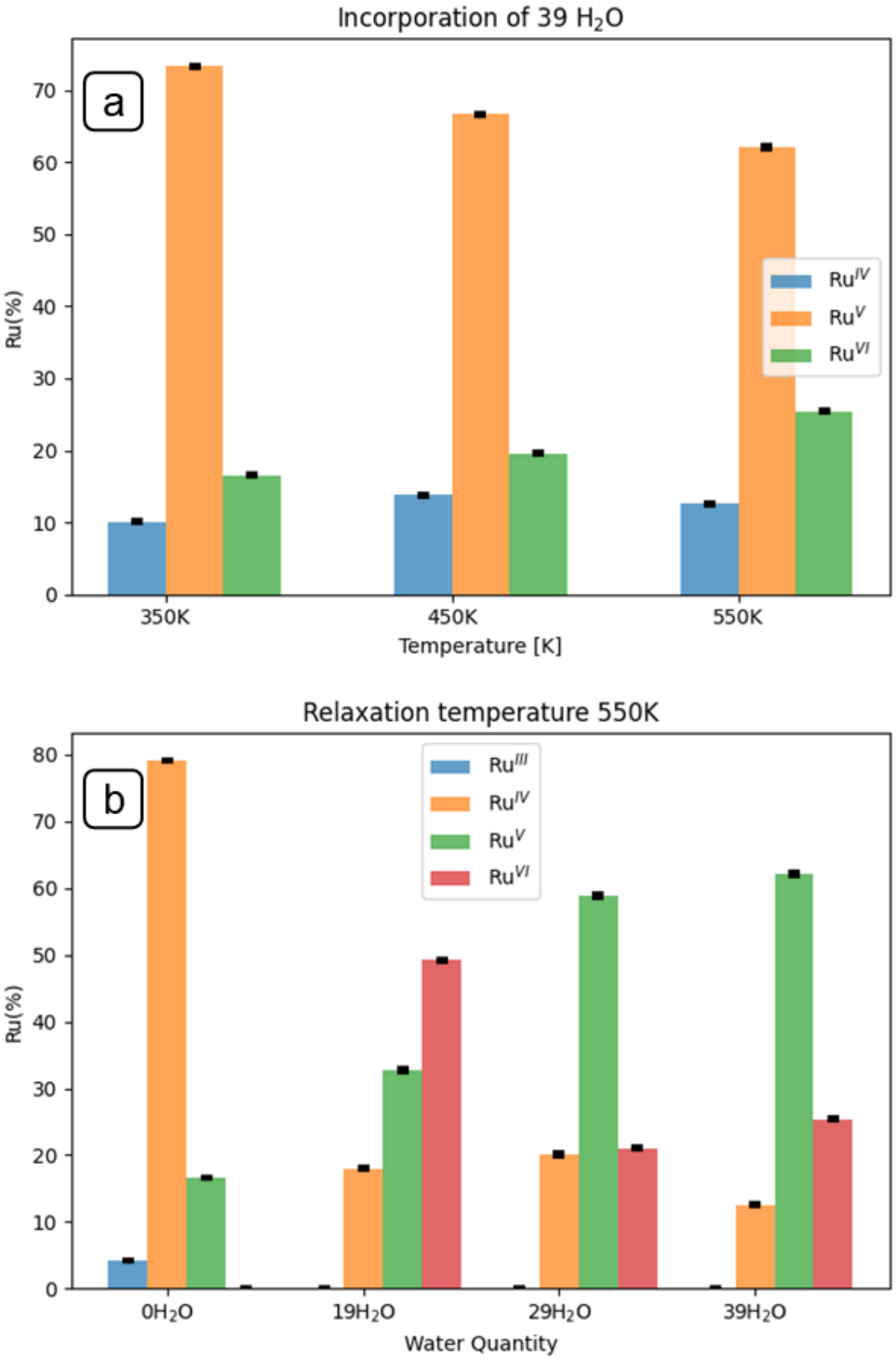

Figure 3: Coordination number of Ru in low−density amorphous hydrated RuO_2. (a) Temperature effect from 350 K to 550 K for a quantity of incorporated water molecules of 39 H_2O. (b) Effect of different quantities of incorporated water molecules, namely (0 H_2O, 19 H_2O, 29 H_2O), and 30 H_2O, while keeping the relaxation temperature fixed at 550 K.

Table 2: Characteristics of amorphous hydrated RuO_2 with low density under different relaxation temperatures and quantities of incorporated water molecules. Interatomic distances and coordination numbers (CNs) were computed from radial distribution function (RDF) analysis over the last 10 ps. $NBO(\%) \times \left(\frac{100}{\text{total number of O}}\right)$ and $OH(\%) \times \left(\frac{100}{\text{total number of Ru}}\right)$.

Relaxation Temperature at 550 K						
H_2O	r_{Ru-O}(Å)	CN_{Ru-O}	$BO(\%)$	$NBO(\%)$	$OH(\%)$	$D(H)\,(\text{cm}^2.\text{s}^{-1}) \times 10^{-6}$
0 H_2O	1.85±0.04	4.21	100	0	0	−−
19 H_2O	1.92±0.04	5.4	88.89	11.11	116.67	2.05 ($\pm 2 \times 10^{-2}$)
29 H_2O	1.90±0.04	5.1	79.00	21.00	116.67	3.89 ($\pm 6 \times 10^{-2}$)
39 H_2O	1.89±0.04	5.1	79.00	21.00	116.67	7.05 ($\pm 4 \times 10^{-2}$)
Incorporation of 39 H_2O						
Relaxation T(K)	r_{Ru-O}(Å)	CN_{Ru-O}	$BO(\%)$	$NBO(\%)$	$OH(\%)$	$D(H)\,(\text{cm}^2.\text{s}^{-1}) \times 10^{-6}$
350 K	1.88±0.04	5.1	85.48	14.52	108.33	1.65 ($\pm 1 \times 10^{-2}$)
450 K	1.89±0.04	5.1	83.05	16.95	100.00	5.00 ($\pm 4 \times 10^{-2}$)
550 K	1.89±0.04	5.1	79.00	21.00	116.67	7.05 ($\pm 4 \times 10^{-2}$)

The diffusion of hydrogen through the pores of hydrous RuO_2 is influenced by the quantity of incorporated water molecules and the relaxation temperature. In our molecular dynamics (MD) simulations, we compute self−diffusion coefficients (D) using Einstein's relation and a three−dimensional material model based on mean square displacement (MSD). The MSD equation is given by $\text{MSD} = \langle \delta r^2 \rangle = \frac{1}{N} \sum_i [r_i(t + t_0) - r_i(t_0)]^2$. After computing MSD, the self−diffusion coefficient (D) is determined as $D = \lim_{t \to 0} \frac{\langle \delta r^2 \rangle}{6t} = \lim_{t \to 0} \frac{\langle \text{MSD} \rangle}{6t}$.

For example, at 39 H_2O loading and 350 K, the diffusion coefficient (D) is 1.65×10^{-6} ($\pm 1 \times 10^{-8}$) cm^2/s, increasing to 5.00×10^{-6} ($\pm 4 \times 10^{-8}$) cm^2/s at 450 K and 7.05×10^{-6} ($\pm 4 \times 10^{-8}$) cm^2/s at 550 K. Similarly, with an increase in the quantity of water molecules at 550 K, the diffusion coefficient (D) becomes 2.05, 3.89, and 7.05×10^{-6} ($\pm 1 \times 10^{-8}$) cm^2/s for 19, 29, and 39 molecular water loading, respectively.

In the same context, using density functional theory (DFT), Ozolin *et al.*[16] found that

proton diffusion in the crystalline state of RuO_2 has the lowest barrier energy on the surface $RuO_2(110)$, with a diffusion coefficient (D) of about $10^{-16}\,cm^2/s$, which is very low compared to what we find in the simulated low−density amorphous hydrous state for any given water quantity. The Arrhenius equation, $\ln(D) = -\frac{E_a}{RT} + \ln(A)$, reveals an activation energy (E_a) of approximately 0.123 eV, where R is the gas constant and T is the absolute temperature. Experimental investigations by nuclear magnetic resonance (RMN) show a variation in activation energy (E_a) with increasing annealing temperatures in the range of 298.15 K to 423.15 K, reaching a minimum of 0.0255 eV at approximately 423.15 K.[13] The proton dynamics in $RuO_2{\cdot}xH_2O$ samples are temperature−dependent, with higher temperatures allowing for easier proton diffusion, consistent with our AIMD simulation results.

Looking now at the structural distribution of species at the pore walls/water molecule interface, we observe the formation of hydrogen bond networks. These networks exhibit a characteristic ring structure, that is the source of a distinct migration pattern for hydrogen through the so−called Grotthuss mechanism. This is illustrated in Figure 4, showing a ring structure involving two water molecules. Connections follows one surface H−bond acceptor BO site (labeled as site 4) being hydrogen bonded to a water oxygen donor atom (site 3), which is oriented to share another hydrogen bond with a neighbouring water molecule (site 2), that in turn is hydrogen bonded with a surface BO site. As a general observation during the AIMD simulations, the adsorbed water molecule donates one of its protons to the neighboring water molecules within the pores of the hydrous RuO_2. Subsequently, these water molecules transfer one of their protons to a BO site, leading to the formation of an OH group. This network of hydrogen bonds enhances proton migration due to the flexibility of the network, allowing for the relaxation of transition states along the migration path. Moreover, distant active sites for hydrogen migration can interact through water forming ring. Similar structural configurations have been observed prior studies, notably at the borosilicate−water interface[26] and in Car−Parrinello AIMD simulations exploring the proton−exchange process between water and a carbamate.[34] Additionally, Merte et al.[35]

employed high−speed, high−resolution scanning tunneling microscopy to investigate proton diffusion on an iron oxide surface. Their research on oxygen−terminated FeO monolayer films formed on Pt highlighted the role of molecular water in accelerating proton diffusion, suggesting the potential importance of water−assisted proton diffusion in various catalytic processes. In a related study, Devanathan et al.[36] investigated proton hopping in a model polymer membrane and observed that the barrier for proton transfer decreases with increasing hydration levels. They considered three hydration levels (λ) of 3, 9, and 15 H_2O/SO_3^-, corresponding to the dry, hydrated, and saturated fuel cell membrane, respectively. The barrier for proton transfer from the SO3$^-$-H3O$^+$ contact ion pair to a solvent−separated ion pair decreased from 0.036 eV for $\lambda = 3$ to 0.013 eV for $\lambda = 15$.

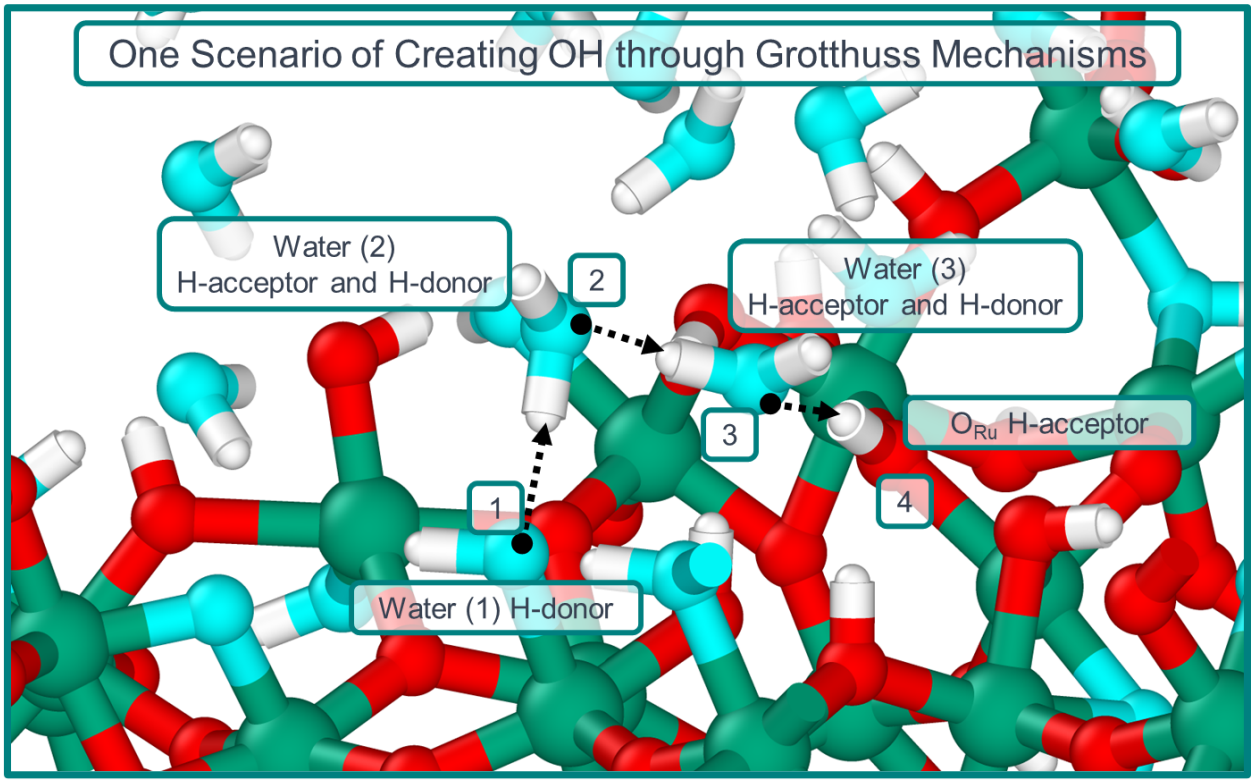

Figure 4: Illustration of hydration mechanisms involving a ring structure connecting the adsorbed H−bond donor water molecule (1), two nearby H−bond acceptor and donor−water molecules (2 and 3), and an H−bond acceptor (4).Green balls represent Ru atoms, red balls represent O atoms initially belonging to RuO_2, blue balls represent O atoms initially belonging to H_2O, and white balls represent H atoms.

In addition to Grotthuss mechanisms, our AIMD simulations unveiled alternative modes

of hydrogen migration, including proton hopping between two adjacent Ru atoms. Specifically, the migration pathway illustrated in Figure 5a (initial state), Figure 5b (transition stage), and Figure 5c (final stage) involves a water molecule adsorbed on one Ru atom, nearby an OH group (NBO type) located on an adjacent Ru atom. This OH group (acting as an H−bond acceptor) subsequently attracts a proton from the adsorbed water (acting as an H−bond donor), completing the process of water creation in a swift duration of 0.03 ps. As the diffusion process continues, we observe that the water molecule created after the proton diffusion (acting as an H−bond acceptor) can further adsorb *via* its oxygen onto another Ru atom. In this capacity, it acts as an H−bond donor to another OH group bound to an adjacent Ru. This additional process is illustrated in Figure 5e (initial state), and Figure 5f (final stage), with a similar duration of 0.03 ps. This mechanism demonstrates the propensity of water dissociation close to neighboring oxygen site being of the NBO type. In a related study, Tilocca and Cormack[37] investigated the water−bioglass interface using *ab initio* (Car−Parrinello) AIMD simulations. They found that during their simulation trajectory, a water molecule dissociates close to NBO sites through a sequence of proton transfers between dissociated water molecules and NBO sites.

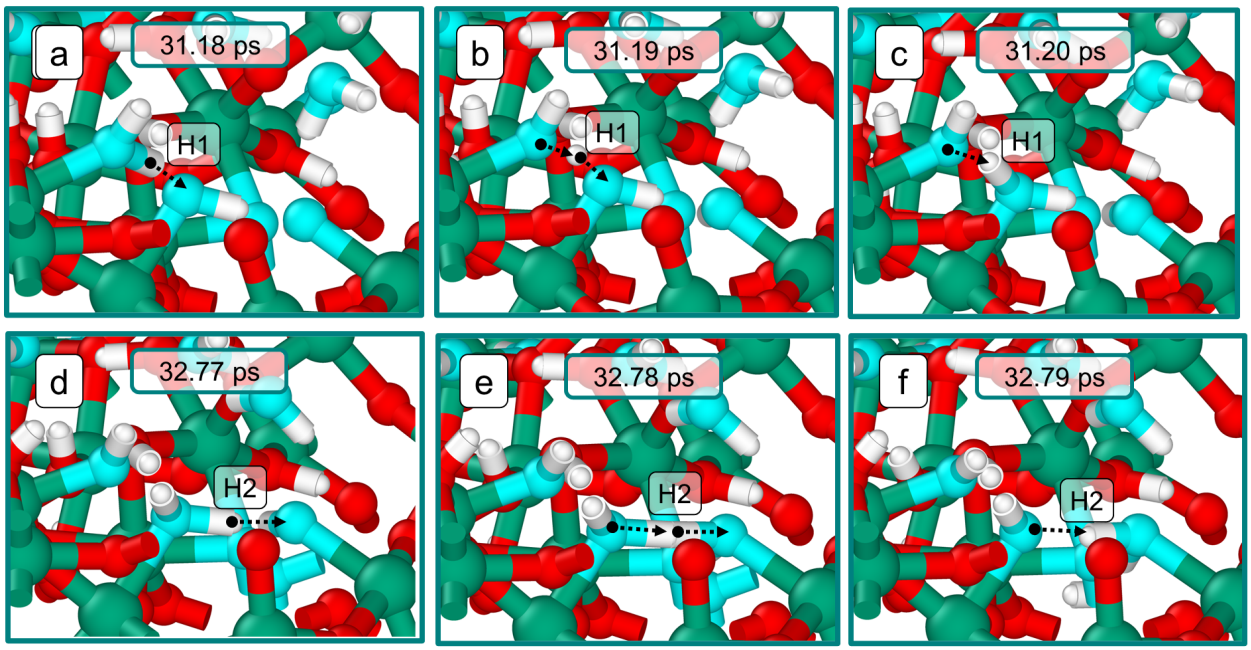

Figure 5: Snapshots illustrating the key stages of protons undergoing spontaneous migration between hydrated sites *via* a hopping mechanism. (a−c) First migration sequence of a proton to form an adsorbed water molecule, which then (d−f) looses one proton at the benefit of another hydrated site nearby, thus forming a new adsorbed water molecule. The depicted case is from a 39 H_2O loaded RuO_2, at 550 K, which is representative across all investigated temperatures. (Green balls represent Ru atoms, red balls represent O atoms initially belonging to RuO_2, blue balls represent O atoms initially belonging toH_2O, and white balls represent H atoms).

Finally, Figure 6 illustrates direct hopping mechanisms between two protonated NBO sites, without water acting as a migration intermediate. This mechanism can lead to the formation of freed or adsorbed water molecules. Importantly, regardless of the water loading , direct proton hopping *via* bridging oxygen atoms, denoted as BO——H ⇒ H——BO, was not observed in the duration of the simulation. This process, however, is likely to occur in the presence of a chain of water molecules. Additionally, there is no Grotthuss mechanism of H diffusion between adjacent NBOs or between NBO and one adjacent BO. Moreover, H can only diffuse from BO to NBO and not in the opposite direction due to the competitive factors favoring NBO in the adsorption of protons when BO is nearby. Finally, BO^{III}, where an oxygen connected with three Ru atoms, does not exhibit any protonic residence.

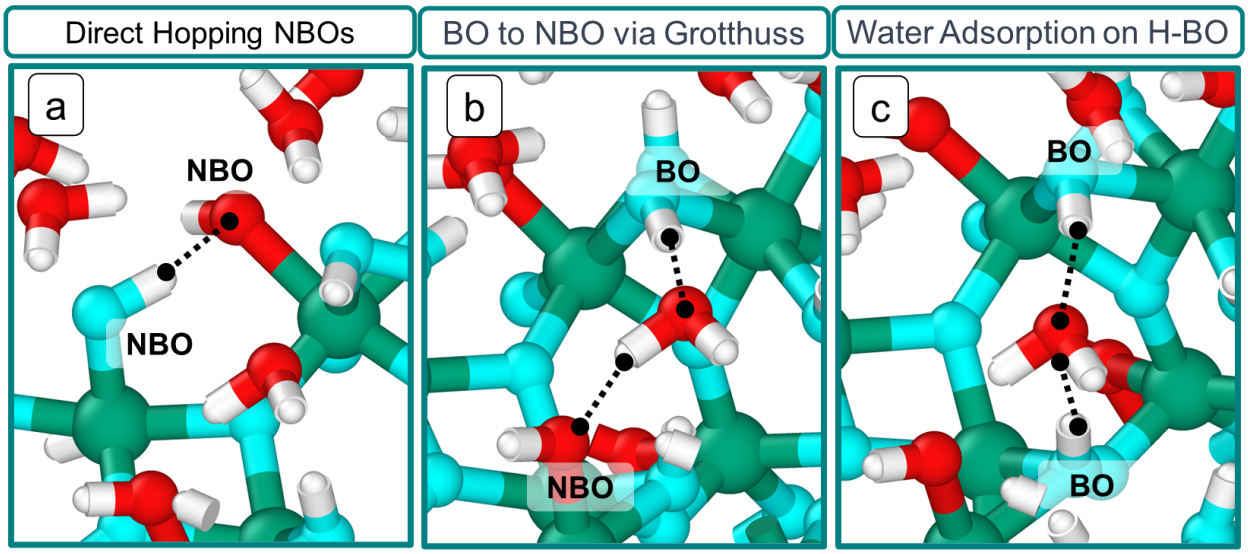

Figure 6: Snapshots representing three dominant forms of proton migration between different kinds of oxygen atoms: (a) proton migration between two H−NBO, (b) proton migration between a bridging oxygen H−BO *via* a Grotthuss mechanism, and (c) the adsorption configuration of water *via* its oxygen towards the bridging oxygen showing the difficulty of proton migration *via* a Grotthuss mechanism. The depicted case is from $RuO_2 \times 39\,H_2O$ at 550 K, which is representative across all investigated temperatures. Green balls represent Ru atoms, red balls represent O atoms initially belonging to RuO_2, blue balls represent O atoms initially belonging to H_2O, and white balls represent H atoms.

Inventory and quantification of hydrogen migration

In this section, we provide an energetic quantification of the various hydrogen migration mechanisms observed through AIMD simulations, as discussed earlier. Determination of the activation energy (E_a) for each mechanism is performed combining DFT and NEB calculations. All mechanisms are conducted using the hydrous $39H_2O$-RuO_2 model system obtained after relaxation at 550 K. We first consider the water dissociation and further migration of hydrogen within the dehydrated structure. This serve as a reference for the hydrated case and a potential case study in which dehydration of the hydrous material would be achieved because of annealing. It is worth noting that such procedures have been experimentally investigated, revealing an intersting optimum in capacitance after annealing at 150 °C. Beyond this temperature capacitance decreased at either lower or higher annealing temperatures.[38] From Table 3, it is shown that water inside the pore dissociates after overcoming an activa-

tion barrier of 0.22 eV. The pathway is illustrated in Figure 7a, in which dissociation leads to the formation of two hydroxyl groups, on NBO and BO sites, respectively.

Table 3: Calculated activation barriers (E_a) and reaction energies (E_{rxn}) in kJ.mol^{-1} for proton diffusion and water dissociation reactions within the pores of dehydrated low−density amorphous RuO_2 (utilizing a single molecule) and hydrated low−density amorphous RuO_2 (using a system with 39 H_2O molecules).

System	**Reaction**	E_a **(eV)**	E_{rxn} **(eV)**
Unhydrated	Water dissociation near two BO^{II}	0.22	0.20
	H−hopping (H−NBO ⇒ BO^{II})	0.33	0.31
	H−hopping (H−BO^{II} ⇒ BO^{II})	0.60	-0.29
Hydrated	Water dissociation near NBO	0.08	0.08
	H−hopping (H−NBO ⇒ H−NBO)	0.06	-0.02
	H−hopping (H−BO^{II} ⇒ H−BO^{II})	0.48	-0.25
	Grotthuss *via* one H_2O (H−BO^{II} ⇒ H−BO^{II})	0.45	0.30
	Grotthuss *via* one H_2O (H−BO^{II} ⇒ H−NBO)	0.32	0.25

Two migration pathways are then investigated. Firstly, the migration from a NBO towards a neighbouring BO^{II} gives an activation energy of 0.33 eV. Secondly, H migration beetwen two BO^{II} sites has an activation energy of 0.60 eV, indicating the prevalence of the NBO site. Since the activation barrier for water dissociation is lower than that of diffusion, it can be argued that molecular water may follow the reverse reaction rather than dissociating and spreading within the pore walls. In addition, the overall reaction energy is positive in this particular case. However, calculation under higher water loading clearly shows preferential water splitting, indicating the self−stabilization of hydration. It is important to note that all reaction energies, being less than 0.3 eV in absolute value, cannot be deeply considered as they fluctuate due to the final possibility or inability to locally form hydrogen bonds. Rather, they signify that all these potential migrations are performed at quasi isoenergy. This, coupled to the low activation barriers calculated, underlines the importance of the density and spatial distribution of the three actors for hydrogen migration, e.g., BO, NBO and water

molecules. No proton diffusion is seen between BO^{III} sites, where oxygen forms a planar surface with three interconnected Ru. In this scenario, diffusion occurrs exclusively in the presence of a water molecule through the Grotthuss mechanism, a phenomenom prominently observed and discussed in the subsequent analysis of the hydrated system.

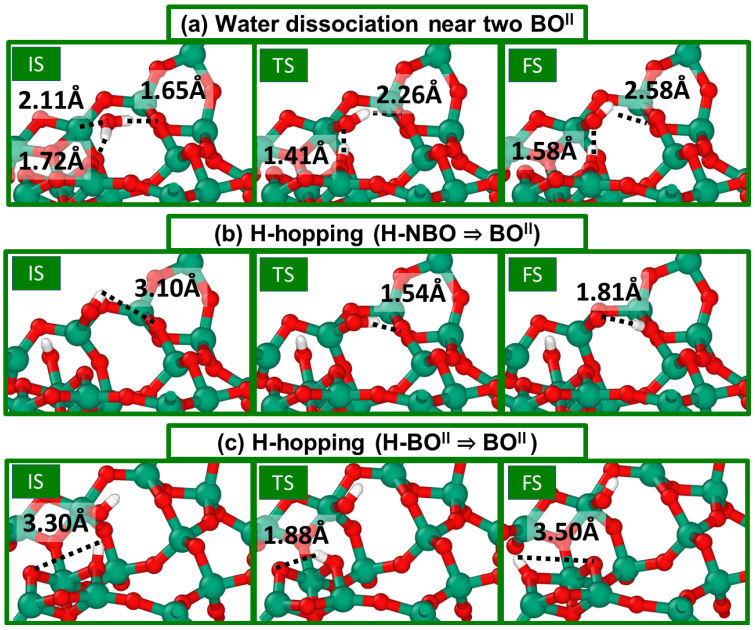

Figure 7: Pathway mechanism snapshots for three important events related to proton diffusion and water dissociation reactions within the pores of unhydrated low−density amorphous RuO_2 (utilizing a single molecule): (a) water dissociation adsorbed *via* its oxygen on Ru^{IV} and close two BO^{II}, (b) H−Hopping diffusion between H−NBO and BO^{II} oxygen sites, and (c) H−Hopping diffusion between H−BO^{II} and BO^{II} oxygen sites. Green balls represent Ru atoms, red balls represent O atoms initially belonging to RuO_2, blue balls represent O atoms initially belonging to H_2O, and white balls represent H atoms.

Now, turning our attention on the hydrated system, as detailed in Table 3 and depicted in Figure 8, water dissociation is quasi barrierless, with an activation barrier of 0.08 eV. This value is lower than that of the dehydrated system by approximately 0.15 eV. This difference could be attributed to the presence of numerous NBO sites and the formation of water molecules rings. Furthermore, migration between two NBO sites leads to the formation of a water molecule adsorbed on one NBO, following a nearly barrier−free pathway of 0.06 eV. This process occurs without the need of an alternative Grotthuss mechanism, suggesting the absence of water molecules between the two oxygen atoms to facilitate diffusion.

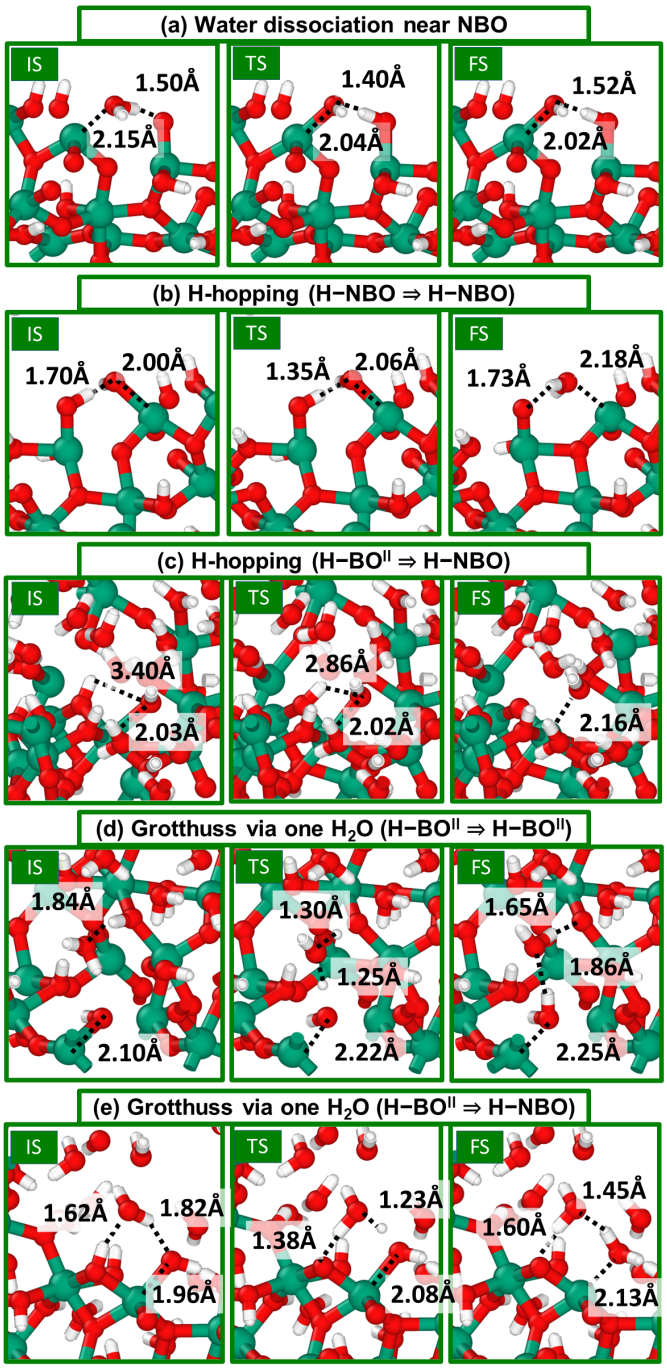

Figure 8: Pathway mechanism snapshots for three important events: proton diffusion and water dissociation reactions within the pores of hydrated low−density amorphous RuO_2: (a) water dissociation adsorbed *via* its oxygen on Ru^{IV} and close NBO, (b) H−Hopping diffusion between H−NBO and H−NBO oxygen sites, (c) H−Hopping diffusion between H−BO^{II} and H−HBO oxygen sites, (d) Grotthuss *via* oneH_2O between H^--BO^{II} and BO^{II}, and (e) Grotthuss *via* oneH_2O between H^--BO^{II} and NBO. Green balls represent Ru atoms, red balls represent O atoms initially belonging to RuO_2, blue balls represent O atoms initially belonging to H_2O, and white balls represent H atoms.

A second event involves H−hopping between two H$-BO^{II}$ without the local presence of water molecules. In this case, the activation barrier is 0.48 eV, significantly higher than that observed between two H−NBOs. This is attributed to the greater freedom degree of the unique Ru−−O bond of NBO sites, facilitating the H−bond donor and H−bond acceptor mechanisms compared to the more constrained H$-BO^{II}$.

In the presence of water between two H$-BO^{II}$ sites, proton diffusion can occur, mediated by the formation of a ring comprising H−bond donor and H−bond acceptor water molecules. Known as Grotthuss diffusion, this process incurs an activation energy of 0.45 eV, nearly identical to the observed activation energy for the direct hopping event between the two H$-BO^{II}$ sites. Furthermore, the existence of water molecules between two hydrated oxygen atoms facilitates the creation of the H_3O^+ compound at the transitional state. Prior investigations using density functional theory calculations and observations from scanning tunneling microscopy (STM) have suggested the involvement of a H_3O^+ transitional state in the diffusion process. The presence of absorbed water intensifies hydrogen migration, presumably through a transitional state involving hydronium ions. The acceleration of hydrogen atom diffusion over solid oxide surfaces is commonly associated with the presence of water molecules. This mechanism differs from the observations made in the case of rutile $TiO_2(110)$, where the dissociation of water plays a crucial role in proton diffusion. Besides, using DFT calculations and comparison with experimental results, Lin et al.[39] observed that proton diffusion in tungsten oxide dihydrate ($WO_3x_2H_2O$), a well−known efficient proton conductor, occurs within the layers of corner−sharing WO^6 octahedra, without the direct involvement of structural water. The calculated barrier for proton migration in $WO_3x_2H_2O$ (0.42 eV) closely aligns with the experimental value derived from the temperature dependence of conductivity (0.36 eV).

It is important to emphasize that within the hydrated system, regardless of the quantity of incorporated water molecules or temperature, no instances were observed where hydrogen could diffuse through a ring formed by H−bond donor and H−bond acceptor water

molecules between two NBO sites. In contrast, a Grotthuss−type migration was observed for hydrogen migration between an H−BO^{II} site and an H−NBO site, a process requiring an activation energy of 0.32 eV, marginally lower than the energy required for migration between two H−BO^{II} sites. It is noteworthy that the direction of hydrogen migration is mainly achievable due to the difficulty of bonding two hydrogen atoms on the BO sites. From these energetically quantified results, hydrogen migration is shown to be always feasible, even though overall configurations stabilize through the complex interplay of the hydrogen bond network that forms upon hydration and water exposure. Also, hydrogen migration is energetically favored when considering NBO sites, which almost annihilate activation barriers, and water, which allows interaction and migration from distant size. In summary, both the statistical insights from molecular dynamics simulation and the migration pathways identified through DFT−NEB calculations emphasize the substantial impact of water and hydroxyl coverage on the performance characteristics of the porous RuO_2. These findings are consistent with the observed decrease in capacitance for hydrous RuO2 submitted to annealing at temperatures exceeding 150 °C, where water loading is compromised due to the opening of the experimental set up to vaporization[38] Along this line, the reduction in capacitance at lower annealing temperatures could be associated with a lower amount of NBO sites at the pore surfaces.

CONCLUSION

This study reports a thorough exploration of the low−density amorphous state of ruthenium dioxide (RuO_2) and its hydration dynamics using advanced computational techniques, aiming to provide new insights into the remarkable supercapacitor performances experimentally observed in hydrous−RuO_2 electrodes. The material's structure and chemical composition are systematically analysed such as porosity formation, ruthenium oxidation states, alterations in coordination numbers with oxygen, and the emergence of local structures involving

OH and water, particularly H bonded to RuO_2 bridging or non− bridging oxygen atoms. This analysis varies with the hydration process, adjusting the initial water loading in the dry porous low−density structure and the temperature, while comparisons are made with fully dense amorphous RuO_2. It is found that full hydration is achieved at all tested initial water loadings and temperatures, leading to the stabilization of molecular water in the pore regions with more than one OH group per Ru atom in the structure. Most importantly, rather than the overall coordination and structural aspects of the obtained hydrous−RuO_2 model system, it is found that the hydrogen motion within the material correlates with the presence of OH species on non−bridging oxygen sites and the existence of molecular water into the pores. Finally, the hydrogen migration mechanisms are quantified utilizing the DFT−NEB technique. For all tested case, relatively low activation energies are calculated for hydrogen transport within the material (all below 0.5 eV). This underscores the significance of chemical sites statistics and spatial distribution (distance making direct hopping unlikely), with the presence of water being crucial for enabling distant hydrogen migration through the Grotthuss mechanism. The results confirm the predominant role of non−bridging oxygen sites, which, in all tested case, significantly reduce activation barriers, making hydrogen migration nearly barrierless (0.06 eV). These findings not only enrich our general comprehension of these intricate processes involved in metal oxide hydration but also contribute to a deeper understanding of electrochemical performance, offering valuable insights into the potential of amorphous hydrous RuO_2 as an advanced electrode material for supercapacitors.

Acknowledgement

The authors gratefully acknowledge the support received from the European Research Council (ERC) under the European Union's Horizon 2020 research and innovation programme (grant agreement No 771793, ERC 3D−CAP). Additionally, we would like to express our appreciation for the generous provision of high−power computing resources by CALMIP for

conducting this research

Competing Interests

The authors declare that there are no conflicts of interest, encompassing both personal relationships and financial factors, which could have influenced the publication of the study presented in this article.

Supporting Information

We present classical molecular details here, further analysis, and spatial coordinations of obtained RuO_2 structures at different states, namely dry RuO_2 amorphous with full density and with low density, as well as hydrated structures for different quantities of H_2O.

References

(1) Simon, P.; Gogotsi, Y. Perspectives for electrochemical capacitors and related devices. *Nature materials* **2020**, *19*, 1151–1163.

(2) Kyerematen, N. A.; Brousse, T.; Pech, D. Microsupercapacitors as miniaturized energy-storage components for on-chip electronics. *Nature nanotechnology* **2017**, *12*, 7–15.

(3) Salanne, M.; Rotenberg, B.; Naoi, K.; Kaneko, K.; Taberna, P.-L.; Grey, C. P.; Dunn, B.; Simon, P. Efficient storage mechanisms for building better supercapacitors. *Nature Energy* **2016**, *1*, 1–10.

(4) Miller, J. R.; Simon, P. Electrochemical capacitors for energy management. *science* **2008**, *321*, 651–652.

(5) Fleischmann, S.; Mitchell, J. B.; Wang, R.; Zhan, C.; Jiang, D.-e.; Presser, V.; Augustyn, V. Pseudocapacitance: from fundamental understanding to high power energy storage materials. *Chemical Reviews* **2020**, *120*, 6738–6782.

(6) Jang, J. H.; Kato, A.; Machida, K.; Naoi, K. Supercapacitor performance of hydrous ruthenium oxide electrodes prepared by electrophoretic deposition. *Journal of The Electrochemical Society* **2005**, *153*, A321.

(7) Zheng, J.; Jow, T. A new charge storage mechanism for electrochemical capacitors. *Journal of the Electrochemical Society* **1995**, *142*, L6.

(8) Zheng, J.; Xin, Y. Characterization of RuO2· xH2O with various water contents. *Journal of power sources* **2002**, *110*, 86–90.

(9) McKeown, D. A.; Hagans, P. L.; Carette, L. P.; Russell, A. E.; Swider, K. E.; Rolison, D. R. Structure of hydrous ruthenium oxides: implications for charge storage. *The Journal of Physical Chemistry B* **1999**, *103*, 4825–4832.

(10) Dmowski, W.; Egami, T.; Swider-Lyons, K. E.; Love, C. T.; Rolison, D. R. Local atomic structure and conduction mechanism of nanocrystalline hydrous RuO2 from X-ray scattering. *The Journal of Physical Chemistry B* **2002**, *106*, 12677–12683.

(11) Dmowski, W.; Egami, T.; Swider-Lyons, K. E.; Yan, W.-F.; Dai, S.; Overbury, S. H. Local atomic structure in disordered and nanocrystalline catalytic materials. *Zeitschrift für Kristallographie-Crystalline Materials* **2007**, *222*, 617–624.

(12) Ma, Z.; Zheng, J. P.; Fu, R. Solid state NMR investigation of hydrous ruthenium oxide. *Chemical Physics Letters* **2000**, *331*, 64–70.

(13) Fu, R.; Ma, Z.; Zheng, J. P. Proton NMR and dynamic studies of hydrous ruthenium oxide. *The Journal of Physical Chemistry B* **2002**, *106*, 3592–3596.

(14) Liu, Y.; Zhou, F.; Ozolins, V. Ab initio study of the charge-storage mechanisms in RuO2-based electrochemical ultracapacitors. *The Journal of Physical Chemistry C* **2012**, *116*, 1450–1457.

(15) Creazzo, F.; Luber, S. Explicit solvent effects on (1 1 0) ruthenium oxide surface wettability: Structural, electronic and mechanical properties of rutile RuO2 by means of spin-polarized DFT-MD. *Applied Surface Science* **2021**, *570*, 150993.

(16) Ozolins, V.; Zhou, F.; Asta, M. Ruthenia-based electrochemical supercapacitors: insights from first-principles calculations. *Accounts of chemical research* **2013**, *46*, 1084–1093.

(17) Jadon, A.; Rossi, C.; Djafari-Rouhani, M.; Estève, A.; Pech, D. Interaction of hydrogen with the bulk, surface and subsurface of crystalline RuO2 from first principles. *Physics Open* **2021**, *7*, 100059.

(18) Jadon, A.; Prabhudev, S.; Buvat, G.; Patnaik, S. G.; Djafari-Rouhani, M.; Estève, A.; Guay, D.; Pech, D. Rethinking pseudocapacitance: a way to harness charge storage of crystalline RuO2. *ACS Applied Energy Materials* **2020**, *3*, 4144–4148.

(19) Jabraoui, H.; Malki, M.; Hasnaoui, A.; Badawi, M.; Ouaskit, S.; Lebègue, S.; Vaills, Y. Thermodynamic and structural properties of binary calcium silicate glasses: insights from molecular dynamics. *Physical Chemistry Chemical Physics* **2017**, *19*, 19083–19093.

(20) Jabraoui, H.; Vaills, Y.; Hasnaoui, A.; Badawi, M.; Ouaskit, S. Effect of sodium oxide modifier on structural and elastic properties of silicate glass. *The Journal of Physical Chemistry B* **2016**, *120*, 13193–13205.

(21) Jabraoui, H.; Charpentier, T.; Gin, S.; Delaye, J.-M.; Pollet, R. Behaviors of sodium and calcium ions at the borosilicate glass–water interface: Gaining new insights through an ab initio molecular dynamics study. *The Journal of Chemical Physics* **2022**, *156*.

(22) Sun, G.; Kürti, J.; Rajczy, P.; Kertesz, M.; Hafner, J.; Kresse, G. Performance of the Vienna ab initio simulation package (VASP) in chemical applications. *Journal of Molecular Structure: THEOCHEM* **2003**, *624*, 37–45.

(23) Ispas, S.; Benoit, M.; Jund, P.; Jullien, R. Structural and electronic properties of the sodium tetrasilicate glass Na 2 Si 4 O 9 from classical and ab initio molecular dynamics simulations. *Physical Review B* **2001**, *64*, 214206.

(24) Perdew, J. P.; Burke, K.; Ernzerhof, M. Generalized gradient approximation made simple. *Physical Review Letters* **1996**, *77*, 3865.

(25) Grimme, S. Semiempirical GGA-type density functional constructed with a long-range dispersion correction. *Journal of computational chemistry* **2006**, *27*, 1787–1799.

(26) Jabraoui, H.; Charpentier, T.; Gin, S.; Delaye, J.-M.; Pollet, R. Atomic Insights into the Events Governing the Borosilicate Glass–Water Interface. *The Journal of Physical Chemistry C* **2021**, *125*, 7919–7931.

(27) Henkelman, G.; Jónsson, H. Improved tangent estimate in the nudged elastic band method for finding minimum energy paths and saddle points. *The Journal of chemical physics* **2000**, *113*, 9978–9985.

(28) Jabraoui, H.; Rouhani, M. D.; Rossi, C.; Esteve, A. First-principles investigation of CuO decomposition and its transformation into Cu 2 O. *Physical Review Materials* **2022**, *6*, 096001.

(29) Haines, J.; Léger, J.; Schulte, O. Pa 3 modified fluorite-type structures in metal dioxides at high pressure. *Science* **1996**, *271*, 629–631.

(30) Haines, J.; Léger, J. Phase transitions in ruthenium dioxide up to 40 GPa: Mechanism for the rutile-to-fluorite phase transformation and a model for the high-pressure behavior of stishovite SiO 2. *Physical Review B* **1993**, *48*, 13344.

(31) Tse, J.; Klug, D.; Uehara, K.; Li, Z.; Haines, J.; Léger, J. Elastic properties of potential superhard phases of RuO 2. *Physical Review B* **2000**, *61*, 10029.

(32) Cotton, F.; Mague, J. The crystal and molecular structure of tetragonal ruthenium dioxide. *Inorganic Chemistry* **1966**, *5*, 317–318.

(33) Le Roux, S.; Petkov, V. ISAACS–interactive structure analysis of amorphous and crystalline systems. *Journal of Applied Crystallography* **2010**, *43*, 181–185.

(34) Pollet, R.; Bonnet, C. S.; Retailleau, P.; Durand, P.; Tóth, É. Proton Exchange in a Paramagnetic Chemical Exchange Saturation Transfer Agent from Experimental Studies and ab initio Metadynamics Simulation. *Inorganic Chemistry* **2017**, *56*, 4317–4323.

(35) Merte, L. R.; Peng, G.; Bechstein, R.; Rieboldt, F.; Farberow, C. A.; Grabow, L. C.; Kudernatsch, W.; Wendt, S.; Lægsgaard, E.; Mavrikakis, M., et al. Water-mediated proton hopping on an iron oxide surface. *Science* **2012**, *336*, 889–893.

(36) Devanathan, R.; Idupulapati, N.; Baer, M. D.; Mundy, C. J.; Dupuis, M. Ab initio molecular dynamics simulation of proton hopping in a model polymer membrane. *The Journal of Physical Chemistry B* **2013**, *117*, 16522–16529.

(37) Tilocca, A.; Cormack, A. N. Modeling the water-bioglass interface by ab initio molecular dynamics simulations. *ACS Applied Materials & Interfaces* **2009**, *1*, 1324–1333.

(38) Majumdar, D.; Maiyalagan, T.; Jiang, Z. Recent Progress in Ruthenium Oxide-Based Composites for Supercapacitor Applications. *ChemElectroChem* **2019**, *6*, 4343–4372.

(39) Lin, H.; Zhou, F.; Liu, C.-P.; Ozoliņš, V. Non-Grotthuss proton diffusion mechanism in tungsten oxide dihydrate from first-principles calculations. *Journal of Materials Chemistry A* **2014**, *2*, 12280–12288.